Video Article

Stress Distribution During Cold Compression of Rocks and Mineral Aggregates Using Synchrotron-based X-Ray Diffraction

Cecilia S.N. Cheung[1,2], Donald J. Weidner[1], Li Li[1], Philip G. Meredith[3], Haiyan Chen[1], Matthew Whitaker[1], Xianyin Chen[4]

[1]Mineral Physics Institute, Department of Geoscience, Stony Brook University

[2]Geological Engineering, Department of Civil and Environmental Engineering, University of Wisconsin-Madison

[3]Rock and Ice Physics Laboratory, Department of Earth Sciences, University College London

[4]Department of Chemistry, Stony Brook University

Correspondence to: Cecilia S.N. Cheung at scheung9@wisc.edu

Abstract

We report detailed procedures for performing compression experiments on rocks and mineral aggregates within a multi-anvil deformation apparatus (D-DIA) coupled with synchrotron X-radiation. A cube-shaped sample assembly is prepared and compressed, at room temperature, by a set of four X-ray transparent sintered diamond anvils and two tungsten carbide anvils, in the lateral and the vertical planes, respectively. All six anvils are housed within a 250-ton hydraulic press and driven inward simultaneously by two wedged guide blocks. A horizontal energy dispersive X-ray beam is projected through and diffracted by the sample assembly. The beam is commonly in the mode of either white or monochromatic X-ray. In the case of white X-ray, the diffracted X-rays are detected by a solid-state detector array that collects the resulting energy dispersive diffraction pattern. In the case of monochromatic X-ray, the diffracted pattern is recorded using a two-dimensional (2-D) detector, such as an imaging plate or a charge-coupled device (CCD) detector. The 2-D diffraction patterns are analyzed to derive lattice spacings. The elastic strains of the sample are derived from the atomic lattice spacing within grains. The stress is then calculated using the predetermined elastic modulus and the elastic strain. Furthermore, the stress distribution in two-dimensions allow for understanding how stress is distributed in different orientations. In addition, a scintillator in the X-ray path yields a visible light image of the sample environment, which allows for the precise measurement of sample length changes during the experiment, yielding a direct measurement of volume strain on the sample. This type of experiment can quantify the stress distribution within geomaterials, which can ultimately shed light on the mechanism responsible for compaction. Such knowledge has the potential to significantly improve our understanding of key processes in rock mechanics, geotechnical engineering, mineral physics, and material science applications where compactive processes are important.

Video Link

The video component of this article can be found at https://www.jove.com/video/57555/

Introduction

The rationale behind the method presented in this article is to quantify the stress distribution within rock and mineral aggregate samples during compression and subsequent compaction. Understanding the compaction in rocks and mineral aggregates is of great importance to reservoir and geotechnical engineering[8,17,18,19,20,28,33]. Compaction acts to reduce porosity, and therefore, leads to an increase in pore pressure. Any such increase in pore pressure leads to a decrease in effective pressure[35]. The consequence is that it will significantly weaken the reservoir rock, and can therefore be subjected to premature failure at lower stress. Some examples of the resulting consequences of inelastic deformation in the subsurface include: failure in sustaining long term production in oil and gas reservoirs[28,33], surface subsidence[8,18,19,20], and alteration of fluid flow patterns[17]. Therefore, a comprehensive knowledge of compaction processes in rocks and mineral aggregates could aid in reducing the possibility of such potentially negative consequences.

The great advantage of using the method highlighted here is that it provides a means to quantify stress distribution internally within a geomaterial[5,6] with respect to the globally-averaged externally applied pressure[12,22]. Moreover, as an *in situ* experiment, the evolution of the stress distribution is time-resolved. The externally applied pressures considered range from relatively low values (tens of megapascals) to high values (several gigapascals). The stress within the sample is measured indirectly by using the atomic lattice spacing within individual mineral grains as a measure of the local elastic strain[5,6]. The atomic lattice spacing is determined with the aid of X-radiation, commonly in either the mode of white or monochromatic X-ray. For the white X-ray mode (*e.g.*, DDIA at 6BM-B beamline of the Advanced Photon Source (APS), Argonne National Laboratory), the intensity of the diffracted beam X-ray beam is determined by not just one, but by an array of 10-element Ge detectors (**Figure 1**) distributed along a fixed circle at azimuthal angles of 0°, 22.5°, 45°, 67.5°, 90°, 112.5°, 135°, 157.5°, 180°, 270°. For the monochromatic X-ray mode, the diffracted pattern is recorded using a CCD detector (*e.g.*, DDIA-30 at 13-ID-D beamline of the GSECARS, APS,

Argonne National Laboratory)[18,23]. Both X-ray modes allow quantification on how the stress varies in different orientations. This approach is fundamentally different from all previous studies of compaction in geomaterials.

In typical compaction studies, a cylindrical sample is compressed by an axial force that is applied across the cross-sectional area by the actuator[25]. Under such conditions, the magnitude of the applied stress magnitude is generally calculated by simply dividing the axial force (measured by a load cell) by the initial cross-sectional area of the sample. It should be noted that this applied stress magnitude is merely an average, bulk value and, as such, does not realistically represent how the local stress state varies, or is distributed, within a complex, heterogeneous, granular material. Detrital sedimentary rocks, which are examples of complex granular materials, are formed by aggregation of mineral grains that are subsequently compacted and cemented through depositional and diagenetic processes[1,7,21,30,31]. These aggregates naturally inherit pores that comprise the void spaces between grains, which are intrinsic from the geometry of grain packing modified by secondary dissolution. Hence, any applied stress is expected to be supported by and concentrated at grain-to-grain contacts, and to vanish at grain-pore interfaces.

In addition to the complexity of stress variation within a granular material, other factors further complicate studying compaction in these scenarios. First, the local stress field is vulnerable to any changes due to microstructural artifacts (*e.g.,* grain shape, preexisting fractures) that are inevitably present within any detrital sedimentary rock. Second, although the magnitude of the applied stress acting upon the sample surfaces can be fully quantified, the distribution of stresses within the sample body remained poorly constrained. An end effect[32] — a boundary effect whereby the average stress is concentrated near the contact between the loading rams and the samples due to interface friction — is well known to be exhibited in cylindrical samples loaded in compression. As an example, Peng[26] demonstrated strain heterogeneity within uniaxially compressed granite samples subjected to a variety of end conditions. Hence, to accurately compute the local stress distribution in granular material, we present the following detailed protocol for performing X-ray diffraction (XRD) experiments on rocks and mineral aggregates, using a multi-anvil deformation apparatus at beamline 6-BM-B of the APS at Argonne National Laboratory.

Protocol

1. Sample Preparation

1. Choose the test and/or reference sample; this can be either a rock core (step 1.2) or a mineral aggregate (step 1.3), depending the focus of the experimental study.
   NOTE: The following method is certainly not the only way to prepare good quality samples (*e.g.,* other machines can be used). However, the sample preparation adopted in the present study is fully illustrated to achieve the goal of accurate replication.
2. **Rock core samples**
   1. Saw a small rectangular slab from a larger sample rock block. Then surface grind the sample slab such that all six surfaces of the slab are flat and perpendicular to their adjacent surfaces.
   2. To minimize any movement of the sample slab during core drilling, start by placing a machine vice (**Figure 2a**) on a working surface that is highly stable. Ensure that all contact surfaces are clean so that non-perpendicularity is not introduced to the setup. Place the sample slab between the vice jaws (**Figure 2a**) and screw the jaws together ensuring that they are just tight enough to secure the sample without damaging it.
   3. Setup a rotary tool with a rotary workstation package as a coring drill press (**Figure 2a**). Insert a 2 mm (inner diameter) coring diamond drill bit into an adjustable chuck of the drill press. Screw and lock the core drill bit to ensure the assembly is stable during drilling.
   4. Turn on the rotary tool and start lowering the drill assembly towards the sample slab.
      NOTE: Heat is produced at the drill bit tip as the drilling progresses. Excess heat could cause the diamonds at the drill bit tip to wear at an accelerated rate. Since the rotary drill press is not equipped with a water cooling system, and since our sample size is in the millimeter range, the drill bit can be cooled by injecting coolant manually onto the contact between the rotating drill bit and the slab.
   5. Drill to the depth of at least 3.25 mm (double of the ideal final height of the sample) so that substantial height is left for end surface preparation afterwards.
      1. If after retracting the drill bit, the drilled core is still attached to the sample slab, then insert the drill bit around the core and wiggle it slowly until the core is detached from the slab.
      2. If the drilled core is already detached and stuck in the interior of the core drill bit, then insert a pin of diameter 1.85 mm from the opposite end to push the core towards the outside for retrieval.
   6. Use wipes to dry the cooling water, and then air dry the retrieved samples for at least 2 h or, if possible, overnight. Clean the ground dust around the core by rolling it on a piece of low adhesive tape. Measure the diameter of the core and prioritize the samples by a diameter closest to 1.9+ mm.
   7. Next prepare for surface grinding of the end surfaces**.**
      NOTE: It is <u>extremely important</u> to have the end surface contacts flat so that the applied load can be evenly distributed across the entire surface area.
      1. Place sand paper under the grinding jig (**Figure 2b**). Start grinding with coarse grit (*e.g.,* 600 grit), progress towards a finer grit, and finish with at least a 1,500 grit. Insert the core into one end of the hole of the grinding jig. Place tape around the core if it does not fit tightly into the hole of the jig.
         NOTE: Ensure the work surface remains clean to ensure perpendicularity.
      2. Insert a pin (diameter of 1.4 mm) into the other end of the hole. Keep holding the pin gently downwards to keep the sand paper and core in contact (**Figure 2b**). Maintain this position and start slowly grinding the core against the sand paper. Take the core out of the jig and check often to see if the final height (1.67 mm) is reached and if the surface is even.
      3. For parallelism, insert the sample back to the jig for further grinding, until it reaches a precision within 0.5°.

8. To assist in deciding on which sample is the best to use, check the overall shape of the samples using a low magnification (2X–8X) microscope. If possible, obtain some microscopic photographs of the samples for documentation as well.

3. **Mineral aggregate samples**
    1. Prepare mineral grains by first grinding a suitably sized sample of rock or pre-existing powder in a pestle and mortar.
        NOTE: This process can be sped up by using a rotatory tool with a grinding head, instead of the pestle.
    2. Use a low magnification microscope to measure the grain size. Continue grinding until the average diameter of the grains is 4 μm.
        1. Suspend the grains in ethanol. Then separate the grains from the ethanol suspension by using a tall decantation column (~20 cm in height) and settling by gravity.
            NOTE: The removal of grains that are smaller and larger than 4 μm (± 0.5 μm), is based on their mass. The gravitational force acting on the grain is given by:

$$F_{gravity} = mg$$

where m is the mass, and g is the acceleration due to gravity. The forces opposing the motion are buoyancy and drag force. The buoyancy force is given by Archimedes' principal:

$$F_{buoyancy} = \rho g V$$

where ρ is the density, and V is the volume of the displaced fluid. The drag force is given by:

$$F_{drag} = C_D \left[\frac{u^2}{2} \right] \rho A_p$$

where u is the particle-fluid relative velocity, A_p is the area of the particle projected in direction of the motion, and C_D is the drag coefficient. By balancing the forces, set the boundary condition at which the grains reach the terminal velocity. Assuming laminar flow conditions, the velocity of the grain v_{grain} is given in the resulting equation known as Stokes' Law:

$$v_{grain} = \sqrt{\frac{\rho - \rho_{ethanol}}{\rho_{ethanol}} \times gd}$$

where d is the diameter of the grain.

3. Extract the ethanol/grain mix at different heights in the column into separate glass beakers, to obtain grains sorted by their grain diameter.
    NOTE: The rate of grain settling depends on its diameter and density.
4. Leave the content in the beakers overnight to air dry. Measure the final average diameter of the grains using a low magnification microscope and select the batch of grains with a diameter closest to 4 μm (for optimal X-ray signals).

2. Cell Assembly Preparation

1. **Load the prepared samples into a standard D-DIA cell assembly (Figure 3a).**
    NOTE: The D-DIA cell assembly was developed under the Consortium for Materials Properties Research in Earth Sciences (COMPRES) multi-anvil cell assembly development project[14]. The following description of the standard D-DIA cell design (under the COMPRES project) can be used for an addition of increased temperature if desired.
    1. Start with a cell assembly cube (6.18 mm edge length; **Figure 3**) on a clean working surface.
    2. Clean an alumina rod (diameter of 1.5 mm, height of 1.46 mm; **Figure 3a**), an alumina ring (**Figure 3a**), and a graphite ring (**Figure 3a**) in an ultrasonic bath. Prepare the end surfaces of the alumina rod flat and parallel to a precision within 0.5° (refer to Section 1.2.7).
    3. Put a piece of tape at one end of the hole of the cube. Use a pair of tweezers to put the two rings around the alumina rod, and insert them all the way down into the hole of the cube, and such that the graphite ring is in contact with the tape.
        NOTE: The alumina ring is used as a separator; the graphite ring is used for electrical conductivity upon higher temperature application (not applied for the cold compression presented in this study).
    4. Mark the corner of the cube to be aligned with the incoming X-ray beam direction (**Figure 4b**).
        NOTE: The tantalum foil is used to obtain better contrast for quantifying the sample volume using radiography during the experiment (Section 3).
        1. Cut a rectangular piece of tantalum foil (1.5 mm x 17 mm). Fold the foil into a U-shape piece (see **Figure 3b** for more details) and place inside the cylindrical space of the cell assembly. To ensure a tight fit between the foil and the edges of the cylindrical space, use a pin (diameter of 1.83 mm) to push onto the foil against the edges to remove any excess space between the two.
        2. Align this U-shaped foil with respect to the X-ray beam direction (**Figure 4a**), and aim to minimize and maximize the 2-D projection of the foil and the samples, respectively.
    5. Lay a piece of rectangular tantalum foil (1.7 mm x 1 mm) on top of the rock core (**Figure 3b**). Make sure the foil is flat, and align the foil such that the length (1.7 mm) of the foil is perpendicular to the X-ray beam direction (**Figure 4a**).
        NOTE: Either a rock core or mineral aggregate can be a "reference sample", depending on the goal of the experimental study. In this particular example, insert the rock core prepared in Section 1.2. as the "reference sample" portion in **Figure 3b**. The purpose of this piece of foil is to provide better contrast of the boundary between adjacent samples.
    6. Carefully pack the mineral aggregate (prepared in Section 1.3) into the cylindrical space with a spatula (the "sample" portion in **Figure 3b**).
        NOTE: Again, either a rock core or mineral aggregate can be a "sample", depending on the goal of the experimental study.
    7. Remove the excess grains adhered to the lateral side of the cylindrical space gently with air if necessary. Use a pin (diameter of 1.83 mm) and a caliper to check if the final height has been reached; leave 1.4 mm in the height for inserting the top alumina rod.

8. Insert another rectangular piece of tantalum foil (1.7 mm x 1 mm). Clean a new set of an alumina rod (diameter of 1.5 mm, height of 1.46 mm), an alumina ring, and a graphite ring (**Figure 3a**) in the ultrasonic bath. Use a pair of tweezers to put the two rings around the alumina rod, and insert them such that remaining space of the cylindrical volume is fully filled with the graphite ring on top.
9. Use a minimal amount of cement (zirconium powder mixed with activator) to seal the alumina rod exposed on both ends of the cube. After the cement is dried, trim the excess tantalum foil that is still exposed outside of the cube for tidiness.

3. Experimental Procedure

NOTE: The following experiment is performed at beamline 6-BM-B (**Figure 4a**) of the APS at Argonne National Laboratory. The experiment performed at 6-BM-B is under white X-ray mode. This beamline is an open beamline and welcomes proposals from scientists, researchers, and students worldwide to perform experiments under its general user program.

1. **Perform the energy calibration of the system by collecting a diffraction pattern for an alumina standard.**
    1. Collect a diffraction pattern by clicking the "start" button on the "12 Element Detector Control Pump" panel.
    2. Analyze the alumina XRD pattern, which contains built-in Cobalt-57 (Co-57) fluorescence peaks, by calculating the average peak position (Horiz X, Vert Y, and Beam Z dimensions) over the different detectors.
    3. Enter the average values as new pedestal positions in the "6motors.adl" panel. Recollect a diffraction pattern and save as an energy dispersive diffraction file (EDF), which constrains the 2-theta angle and the correlation function between the detector channel and X-ray energy for each of the 10 detectors.

2. Remove the alumina standard and collect an open press X-ray spectrum by clicking the "start" button on the "12 Element Detector Control Pump" panel (with an exposure time of 500 s, to optimize signal-to-noise ratio) to measure the diffraction of the background without any sample assembly.
3. Clean the anvils (truncation edge length of 4 mm) with acetone and use a portable vacuum cleaner to remove all debris from previous experiments. Insert the sample assembly prepared in Section 2 into the center of the experiment setup that consists of four, X-ray transparent, sintered diamond and two tungsten carbide (top/bottom) anvils (**Figure 4b**).
4. Slowly lower the opposing pairs of lateral anvils simultaneously. Use a level to check if the anvils are leveled. Gently push the anvil to adjust the alignment until it is all leveled. The bottom and four lateral anvils should now all be in contact with the sample assembly. Release the safety latch and insert the spacer (**Figure 4a**).
5. Close the hutch and enable the shutter to allow the X-ray beam to enter the hutch.
6. In the "low-pressure pump panel" (labeled as the pump motor controller module in **Figure 5**), turn the "low-pressure pump" button ON and push the "up" button next to the "top ram" label to move the top ram to the top, against the spacer (**Figure 4a**). With the aid of real-time X-radiographic imaging (**Figure 5**), start moving the bottom ram up slowly and carefully until the anvils start to appear in the radiograph. "Leave a very fine gap" such that the sample is not overloaded initially before the experiment.
7. **Turn off all the controls on the low-pressure pump controller module (Figure 5) and close the "pressurize" valve before starting to compress with the high-pressure hydraulic pump.**
    NOTE: The high-pressure pump is controlled using EPICS-based software (**Figure 5**). EPICS is a non-commercial set of open source software tools, libraries, and applications developed by Argonne National Laboratory.
    1. Move the sample position in the Z direction (parallel to the beam) using the "jog" button in the "6motors.adl" panel such that the center of the sample in the ImageJ EPICS area detector plugin software panel aligns with the diffraction focus mark on the screen. This minimizes parasitic diffraction and optimizes the signal-to-noise ratio.

8. Collect diffraction spectra by clicking the "start" button on the "12 Element Detector Control Pump" panel for the core and the aggregate ("jog" button along pedestal Z to move between samples) separately, each with an exposure time of 500 s, at ambient conditions. On the "NDFileTIFF.adl" panel, click the "capture-start" button to capture a radiograph (**Figure 5**) of these samples with an exposure time of ~6 ms.
9. Drive the anvils inwards by wedged guide blocks running on the hydraulics pump by starting the motor. In the "SAM-85 Press Load Control" window (**Figure 6**), set the target load to 50 tons. Turn the feedback on, with the upper limit of the speed control set to 7 (the slowest compression possible).
    NOTE: The press load and speed can be changed depending on the target pressure and the speed of the compression. The maximum press load to avoid the breakage of anvils is 100 tons.
10. Use the "Diffraction-Imaging-Scan-Prosilica" panel (**Figure 7**) to set up an automatic data collection by defining the desired locations of the core (*e.g.,* Press X = 20.738 mm, Press Y = 4.3 mm) and the aggregate (*e.g.,* Press X = 20.738 mm, Press Y = 4.8 mm) for diffraction (with preset exposure times of 500 s) and X-radiographic imaging. Set the cycles required to 0 such that this data collection will repeat continuously. Click "start" to start the data collection.
    NOTE: As the compression progresses, the sample will move upwards, so new desired locations should be updated accordingly.
11. After reaching the target load of 50 ton, click the stop button to stop the automatic data collection in the "Diffraction-Imaging-Scan-Prosilica" panel (**Figure 7**). In the "SAM-85 Press Load Control" window, decompress the sample by setting the lower limit of the speed control to -10 and change the target load to 0 ton.
12. After unloading, collect the diffraction spectra for the core and the aggregate separately, by clicking the "start" button on the "12 Element Detector Control Pump" panel; use an exposure time of 500 s for both the core and the aggregate. On the "NDFileTIFF.adl" panel, click the "capture-start" button to capture a radiograph (**Figure 5**) of these samples with an exposure time of ~6 ms.
13. In the low-pressure pump panel (labeled as the pump motor controller module in **Figure 5**), open the "pressurize valve". Push the "low-pressure pump – on" button. Press the "down" buttons both next to the "top ram" and "bottom ram" labels to move both the top and the bottom rams downwards until the green "Down" light becomes illuminated, then stop driving both rams.
14. In the "low-pressure pump" panel, press the out button near the "spacer block" label to move the spacer arm to the "out" position, and then press the "up" button near the "top ram" label to drive the top ram up until the safety lock engages. Turn all the controls off in the pump motor controller unit (**Figure 5**) afterwards. Slowly and manually move the lateral anvils outwards and remove the sample assembly.

Representative Results

We show one representative result example from an XRD experiment (experiment SIO2_55) run in the multi-anvil press at 6BM-B on a compound quartz aggregate[5,6] and novaculite core sample[6]. The grain sizes of the quartz aggregate and novaculite are ~4 µm and ~6–9 µm, respectively[5,6]. Selected diffraction spectra collected during this experiment are illustrated in **Figure 8**. At ambient pressure, the diffraction spectra from the quartz aggregate and the novaculite are essentially indistinguishable (experiment SIO2_55peak2-Set1 **Figure 8**). Specifically, the relative intensities as well as the widths and positions of all the diffraction peaks are indistinguishable between the two geo-materials. During subsequent compression, the peak width remains unchanged for the novaculite with increasing pressure. In contrast, however, the peak width broadens substantially for the quartz aggregate. **Figure 8** highlights the evolution of the quartz aggregate peaks with increasing pressure; both axial and transverse peaks broaden substantially with increasing pressure. The novaculite peak at zero pressure is also plotted in **Figure 8** for comparison. As the pressure is increased, the peak position (*i.e.,* the centroid of the peak) shifts to higher energy for the quartz aggregate (simultaneously, the novaculite peak shifts to high energy, however, for simplicity, it is not shown in this figure). Higher energy is equivalent to lower d-spacing but, for consistency, the low d-spacing edge of the peak is referred as the high-energy or high-pressure side in this article. At pressures higher than P = ~0.9 gigapascals (GPa) (experiment SIO2_55peak2-Set9 in **Figure 8**), the peak broadens remarkably with increasing pressure for quartz aggregate on the high-energy side, while essentially not changing on the low-energy side; this results in an asymmetric peak evolution. The quartz aggregate peak appears to continue broadening, in both the axial and transverse directions, even at the highest pressures achieved in this experiment of P = ~5.6 GPa (experiment SIO2_55peak2-Set15 in **Figure 8**). In contrast, the novaculite peak remains essentially the same shape as that at zero pressure throughout (note that the novaculite peak at zero pressure is shown throughout **Figure 8** for simplicity).

Since the peak position is an indicator of how close the lattice planes are to each other, a material that contains grains with widely distributed lattice spacings will produce a broadened diffraction peak, and vice versa. In essence, a broadened peak is a convoluted signal of the distribution of lattice spacings in the sample and the instrument response[13]. After deconvolution, a wide distribution of lattice spacings essentially implies a larger strain variance deviated from the mean strain within the sample. This strain heterogeneity within the sample is a result of a stress heterogeneity; hence, the broadening of the diffraction peaks can be used to reveal the microstress distribution (differential stress) in the sample[41]. The micro-stress is estimated by quantifying the width of the peak measured at half of the maximum peak height, commonly referred as "full width half maximum" (FWHM) of the diffraction peak. As an illustration, FWHM is marked as a green horizontal line between two vertical lines constraining the upper and lower energy bounds for experiment SIO2_55peak2-Set1 in **Figure 8**. The FWHM is quantified by the difference between the two energy bounds (*i.e.,* ~0.4 kiloelectron volt (keV) in this particular example). If there is no detectable peak broadening due to change in the grain size ($W_d^2 = 0$; see the Discussion for more details), the peak broadening due to strain (W_s^2) is the subtraction of the total observed FWHM (W_O^2) and the response due to the instrumentation (W_i^2). The response due to the instrumentation can be calculated from the open press spectra (Section 3.1.1). The broadening due to strain (W_2) can be measured in unit of length of lattice spacing,

$$Strain = \frac{W_s}{d}$$

where *d* is the hydrostatic lattice spacing. Differential stress is given by,

$$Differential\ stress = E \times \frac{W_s}{d}$$

where *E* is the Young's modulus (the Voight-Reuss-Hill Average of Young's modulus for quartz is adopted in this calculation[34]). For special case, if the stress in the grains of the sample can be represented by a Gaussian distribution, then half of the grains within the sample will be at a differential stress exceeding this mean value[41,42]. The remaining half of the grains will be at a differential stress below this mean value.

The differential stress, as illustrated in **Figure 9**, is determined by using the peak broadening method (E × Ws/d)[41], for both the quartz aggregate and the novaculite as a function of pressure. Although the plotted values are calculated from only the [101] peak (which is the diffraction peak corresponding to the reflection of the [101] crystallographic planes), it should be noted that the other peaks yield similar results. The novaculite peaks show virtually no broadening and hence reflects that novaculite has accumulated only a modest amount of differential stress. On the other hand, the quartz aggregate shows extremely large differential stresses in both the axial and transverse directions. Moreover, there is twice the amount of the differential stress in the transverse direction than that in the axial direction. In other words, the transverse direction is supporting a significantly higher load as compared to the axial direction, since the load is the driving force for the differential stress. It should be noted that the differential stress ('microstress'), calculated using the above peak broadening method[41], reflects the local grain-to-grain interactions and is not influenced by sample geometry. Such advantages are beneficial over stress ('macrostress') calculated using lattice spacings[35].

As noted earlier, at a relatively low pressure, the diffraction peaks for the quartz aggregate started to broaden asymmetrically. As pressure increases, such asymmetry becomes increasingly more significant. Effectively, how the peak shape evolves demonstrates great similarity to that reported for diamond powder under cold compression[40]. High strength granular materials can support a large load on a portion of the grains, while the rest of the grains support a relatively small number of loads, or at any rate support lower normal stresses in certain directions. A conspicuous feature shown in **Figure 8** is that the low-energy sides of both the axial and transverse quartz aggregate peaks shift by a very small amount relative to the larger shifts observed for the high-energy sides. This implies that considerable amount of the grains remains stress-free in both directions. This can occur only if there are significant number of grains with at least a part of their surface area bounded by voids supporting zero pressure, even at the highest applied pressure in this experiment.
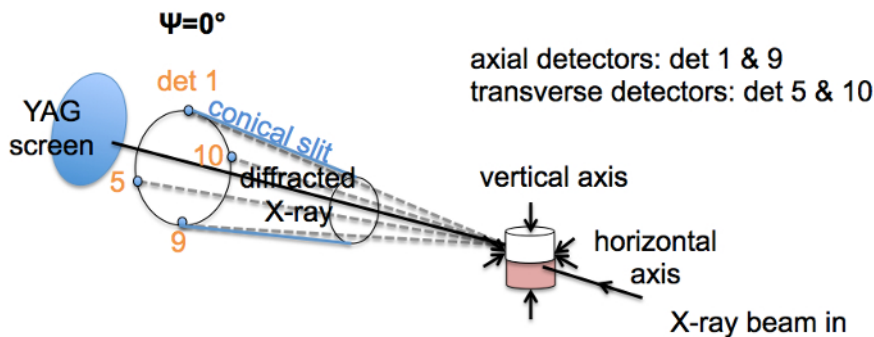
Figure 1: A horizontal white X-ray beam is projected through the sample assembly, perpendicular to the cylindrical axis of the cell. The intensity of the diffracted beam X-ray beam is determined by not just one, but an array of 10 detectors distributed along a fixed circle at azimuthal angles of 0°, 22.5°, 45°, 67.5°, 90°, 112.5°, 135°, 157.5°, 180°, and 270° (Only detectors 1, 5, 9, and 10 are indicated in this diagram, which are the detectors on which our analysis is based on). These detectors allow the quantification of how stress varies in different orientations. This figure has been modified from Burnley and Zhang[2], Burnley[3], and Cheung et al.[6] Please click here to view a larger version of this figure.
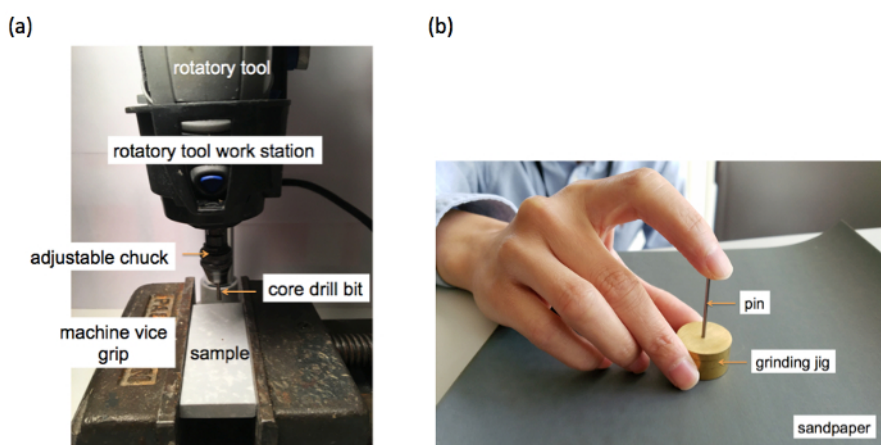
Figure 2: Sample Preparation. (**a**) Core drilling using a rotatory tool with the rotatory workstation package setup as a coring drill press. (**b**) Surface grinding of the end surface of the core sample with a grinding jig (a metal cylinder with a drilled hole). Please click here to view a larger version of this figure.
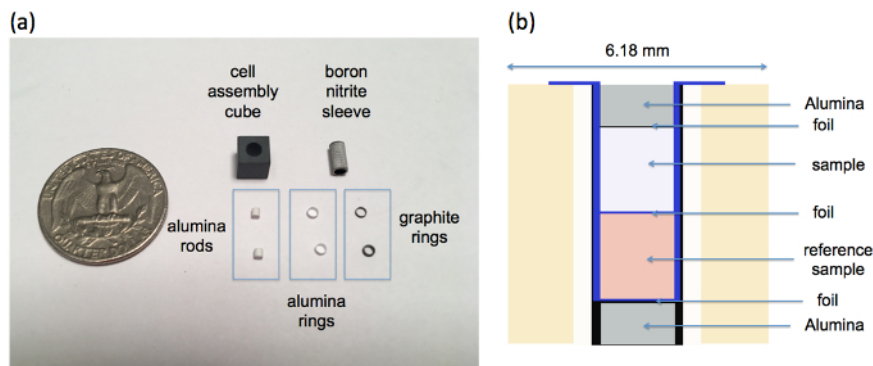
Figure 3: D-DIA cell assembly parts and schematic diagram of cell assembly. (**a**) A set of D-DIA cell assembly with individual components: cell assembly cube (6.18 mm edge length), boron nitrite sleeve, two alumina rods (diameter of 1.5 mm, height of 1.46 mm), two alumina rings, and two graphite rings. Note: 25-cent coin for scale. (**b**) A schematic diagram inside a cell assembly cube. Note that the tantalum foil is shown in a blue color. It consists of one piece folded in a "U" shape and another two linear pieces separating the cell components. This figure has been modified from Cheung et al.[6] Please click here to view a larger version of this figure.
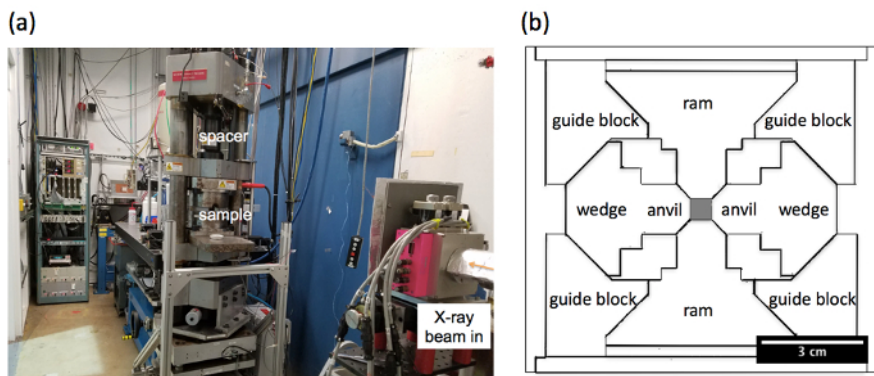
Figure 4: Sample assembly placed in the center of the anvils driven inward simultaneously by two wedged guide blocks within a 250 ton hydraulic press at 6-BM-B hutch. (**a**) The sample assembly is compressed by the anvils driven simultaneously by a wedged guide block pressurized by the hydraulic press. A spacer is inserted to fill up the gaps in the press after the safety latch is removed. (**b**) The schematic diagram shows a side view of a cube-shaped sample assembly (shaded in grey), which is at the center, to be compressed by a set of four, X-ray transparent, sintered diamond, and two tungsten carbide (top/bottom) anvils. Please click here to view a larger version of this figure.
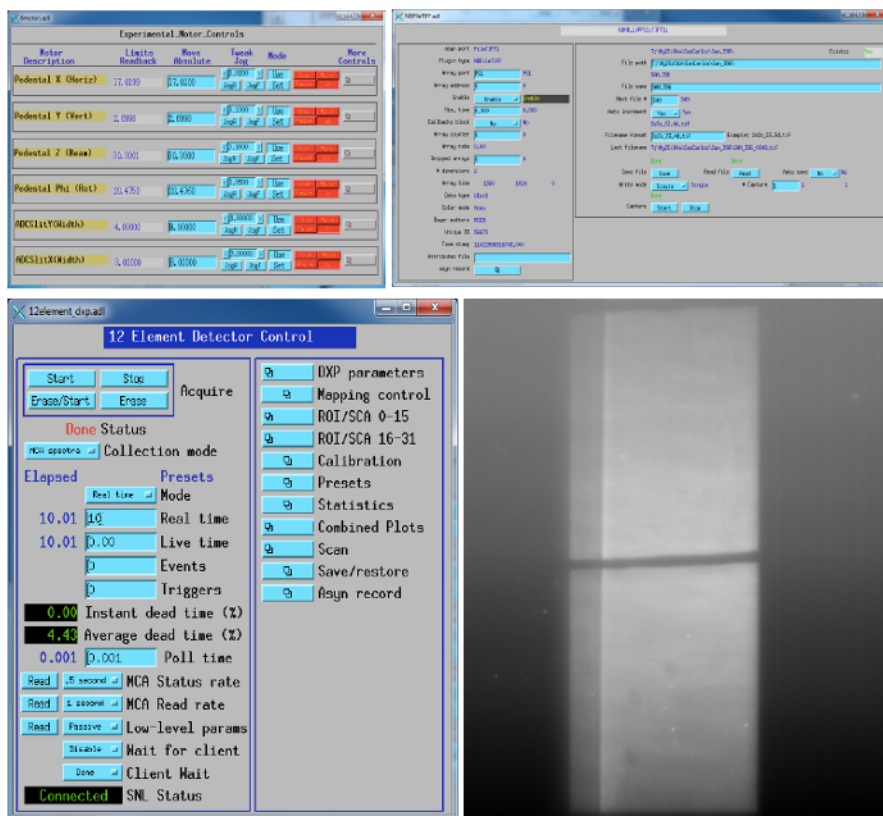
Figure 5: The layout of a pump motor controller module, commercial software package, and codes for instrument control and data acquisition, and radiography at the end station of 6-BM-B. During the compression experiment, first use the pump motor controller module to close any large gaps between the anvils and the press. Then switch to the software interface for controlling using the hydraulic pump. Both can be aided by visually observing the radiograph captured by a camera. Please click here to view a larger version of this figure.
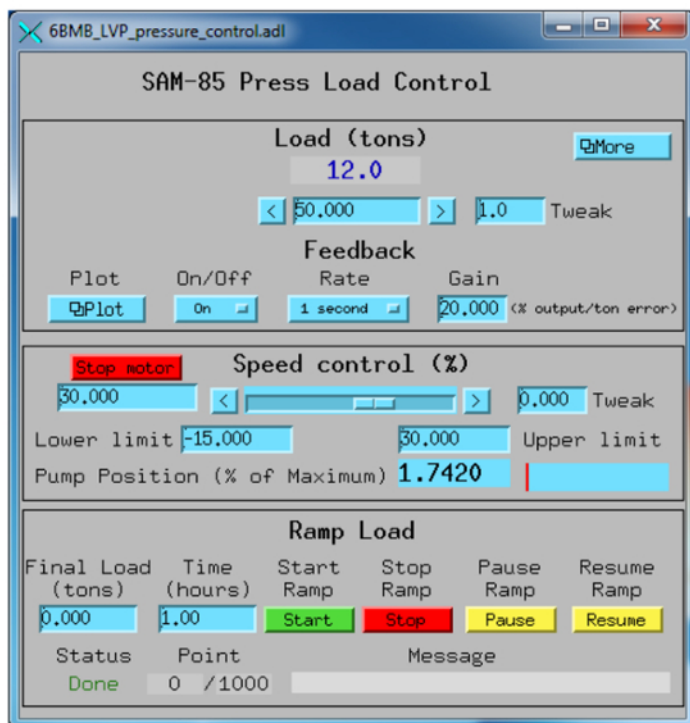
Figure 6: "SAM-85 Press Load Control" window [screenshot]. After switching to the software interface, set the target load to 50 ton in the "SAM-85 Press Load Control" window. Turn the feedback on, with the upper limit of the speed control set to 7 (slowest compression possible) (highlighted in orange). Please click here to view a larger version of this figure.
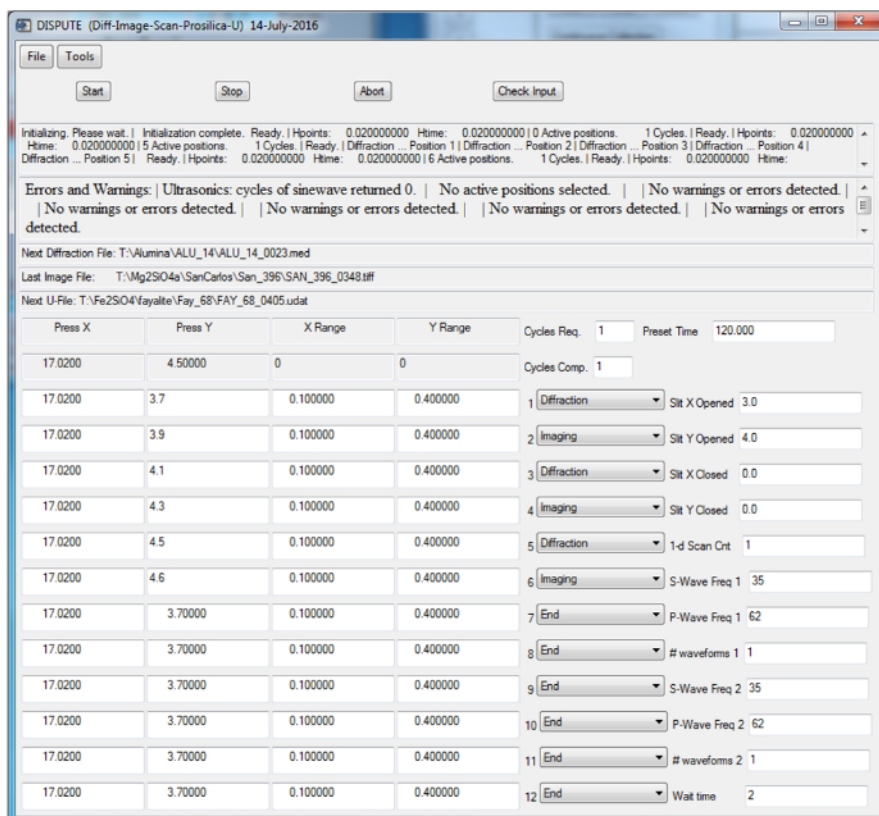

Figure 7: "Diffraction-Imaging-Scan-Prosilica" window screenshot. Set up an automatic data collection by defining the desired locations of the core (*e.g.,* Press X = 20.738 mm, Press Y = 4.3 mm) and aggregate (*e.g.,* Press X = 20.738 mm, Press Y = 4.8 mm) for diffraction (with preset exposure times of 500 s) and X-radiographic imaging. Please click here to view a larger version of this figure.
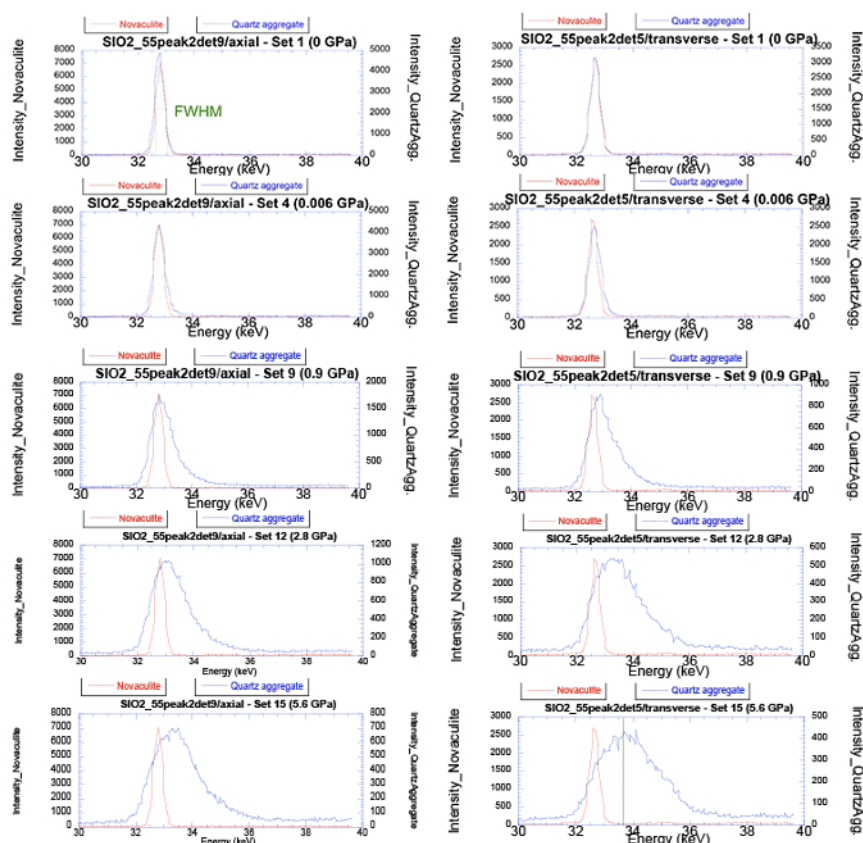
Figure 8: Evolution of the [101] peak for solid grains within quartz aggregate ("quartz agg.") (blue) peaks at selected pressures against the crystallites within the novaculite peak (red) at zero pressure. Both axial (left column) and transverse (right column) directions (experiment SIO2_55) are shown for comparison. This figure has been modified from Cheung et al.[6] Please click here to view a larger version of this figure.

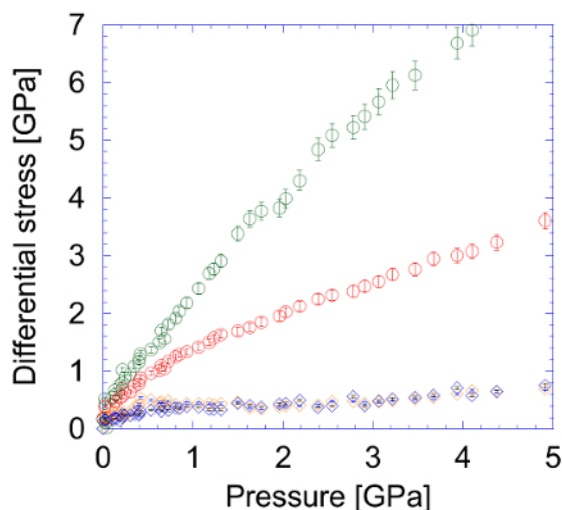**Figure 9: Differential stress.** Differential stress, determined by using the peak broadening method (E×W_S/d), for both the solid grains within the quartz aggregate and the crystallites within the novaculite as a function of pressure. The error bars, calculated using standard deviation, are also plotted as reference. Each data point is the result of an average between [101] and [112] peaks. This figure has been modified from Cheung et al.[6] Please click here to view a larger version of this figure.

Discussion

We present the detailed procedure for carrying out XRD experiments using the multi-anvil cell at 6-BM-B. Perhaps the most critical, and yet most challenging, steps in the above protocol involve optimizing the quality of the sample. Such importance on sample quality applies to almost all rock and mineral deformation experiments. Firstly, it is critical for the end surface of the rock cores to be flat, with both ends parallel to each other and at the same time, perpendicular to the cylindrical surface. That will ensure the external force applied through the anvils is distributed more evenly through the entire end surface of the sample. Other than the end surfaces, the outline of the cylindrical surface attained by the sample is also important because of the geometric assumption in the sample volume calculation.

As highlighted in a note in Section 1, it is important to reemphasize that the presented method is certainly not the only protocol to prepare good quality samples and other equipment can be used to obtain similar quality. Such flexibility in protocol is also applicable to cell assembly preparation (Section 2). In fact, numerous practical or creative modifications can be applied. For example, many components within the cell assembly (*e.g.,* tantalum) can be substituted with similar materials of lower cost. Moreover, modification can be made depending on the aim of the experiment. For instance, the presented method can be extended to incorporate increased temperature. The experimental procedure (Section 3) can be modified depending on the desired hypothesis, parameter (*e.g.,* ultrasonic wave propagation[44,45]), and data quality (*e.g.,* XRD collection time). In general, the experimental procedure is straightforward; however, a note on troubleshooting is discussed here for successful experimentation. Although data collection is automated during compression, it is advised to plot the XRD data regularly to ensure that the data collection is occurring at the desired location. An explanation for why the phase of the XRD data changes abruptly, is that as the compression progresses, the sample may have shifted upwards (Section 3.1.10) and away from the original location. Instead of the sample itself, the XRD collected is diffracted from the foil or other components of the cell assemblies. In this case, new desired locations for XRD data collection should be updated accordingly (see Section 3.1.10). If this is not the case, it is likely that the phase of the sample has been transited.

The main limitation of the method presented here is that XRD signals are optimal for samples with fine grain sizes. The X-ray size is limited by front-end slits, which is usually 100 x 100 μm^2. When grain size is as large as 100 μm, the diffraction pattern may become a single crystal diffraction, which will appear as a single peak in the data collection: this loses the desired resolution for the experiment. Many natural detrital sedimentary rocks have grain sizes that are significantly larger than this narrow range. For example, sandstone, by definition, has a grain size ranging from 62.5 to 2,000 μm: hence, besides transmitting only a poor XRD signal, the limited volume of the measurement cell means that it may be impossible to accommodate a representative sized sample of such materials. Unless the sample of interest naturally has an average grain size within the optimal range (*e.g.,* siltstone), the only testing option may be to grind the test material into a mineral aggregate, following the protocol described in Section 1.2, rather than drilling a rock core. In this way, the resulting XRD signal is resolved optimally, but the test material is reduced to a non-cohesive aggregate and its grain size is reduced. Another limitation to this protocol is also closely related to the grain size of the sample. To determine the microstress (differential stress) distribution in the sample using FWHM of the diffraction peak, Gerward *et al.*[11] reported that the total observed FWHM (W_O) is a composite of peak broadening due to strain, grain size, and the instrument:

$$W_o{}^2 = W_s{}^2 + W_d{}^2 + W_i{}^2$$

where the subscript s refers to strain, d to the grain size, and i to the instrument. After subtraction of the peak broadening due to the instrument ($W_i{}^2$), known from the background spectrum obtained in Section 3.1.1, the peak broadening due to strain ($W_s{}^2$) is equal to the observed peak broadening ($W_O{}^2$) minus the peak broadening due to grain size ($W_d{}^2$). However, Weidner[41] noted that unless a significant fraction of grains is smaller than 100 nm, the effect of grain size would not be detected by the energy dispersive detector. Hence, it is worthwhile to measure the postmortem grain size using the scanning electron microscope. Alternatively, it could also be confirmed by comparing the XRD peak width before and after loading.

The advantage of using the method above over other methodologies is that it can provide the quantification of how stress is distributed in different orientations within a geomaterial. The stress within the sample is measured indirectly by using the atomic lattice spacing within individual grains as a measure of the local elastic strain. Such an approach is fundamentally different from previous compaction studies. In conventional compaction studies, a cylindrical sample is compressed by an axial force across the cross-sectional area. The applied stress magnitude is then estimated simply by dividing the axial force (measured by a load cell) by the initial cross-sectional area. It should be noted, however, that the applied stress magnitude measured in this way is merely an average, bulk value and, as such, does not realistically represent how the local stress state varies within a complex, heterogeneous, granular material.

Compaction study using the above presented method allows successful quantification of the stress distribution within geomaterials, which ultimately reveals details about the process of compaction. Such knowledge has great importance in application to rock mechanics, geotechnical engineering, mineral physics, and material science. For future directions and applications on rock mechanics and mineral physics experimental investigation, it will be extremely useful to develop and incorporate a pore fluid system into the current setup. There are previous reports of the presence of free water percolating in the Earth's crust down to depths of more than 20 km in depth[10,24]. The presence of a pressurized pore fluid in porous samples would enable better simulation of realistic conditions at depth in the crust, and therefore enable better predictions of mechanical properties and stability. Moreover, recent research[29] indicated that fluid flow in porous media is not as stable as previously suggested by Darcy's Law. This opens up an exciting new direction in investigating how pore fluids permeate through geo-materials in anisotropic and inhomogeneous ways. Moreover, incorporating pore pressure, into the setup would allow simulation of hydraulic fracturing experiments using XRD; an important and timely application to the current increased interest in shale gas production. Instead of 2-D radiography, these future applications would be best aided with an image visualization using 3-D X-ray tomography. These suggested future directions are encapsulated within plans for a new multi-anvil cell currently under installation at the National Synchrotron Light Source II (NSLS-II) X-ray Power Diffraction (XPD) beamline at Brookhaven National Laboratory (BNL).

Disclosures

The authors declare no conflict of interest.

Acknowledgements

References

1. Bjørlykke, K. Relationships between depositional environments, burial history and rock properties. Some principal aspects of diagenetic processes in sedimentary basins. *Sedimentary Geology.* **301**, 1-14 (2014).
2. Burnley, P.C., Zhang, D. Interpreting in situ X-ray diffraction data from high pressure deformation experiments using elastic-plastic self-consistent models: An experiment using quartz. *J. Phys. Condens. Matter Solid Earth.* **20** (28), 285201 (2008).
3. Burnley, P.C. Elastic plastic self-consistent (EPSC) modeling of plastic deformation of fayalite olivine. *American Mineralogist.* **100** (7), 1424-1433 (2015).
4. Chen, J., Li, L., Weidner, D.J., Vaughan, M.T. Deformation experiments using synchrotron X-rays: in situ stress and strain measurements at high pressure and temperature. *Phys. of the Earth and Planetary Interiors.* **143**, 347-356 (2004).
5. Cheung, S.N.C. Experimental deformation in sandstone, carbonates, and quartz aggregate. Ph.D. Thesis, *State University of New York at Stony Brook.* (2015).
6. Cheung, S.N.C. *et al.* Stress distribution during cold compression of a quartz aggregate using synchrotron X-ray diffraction: observed yielding, damage, and grain crushing. *J. Geophys. Res. Solid Earth.* **122**, 2724-2735 (2017).
7. Croizé, D., Ehrenberg, S.N., Bjørlykke, K., Renard, F., Jahren, J. Petrophysical properties of bioclastic platform carbonates: implications for porosity controls during burial. *Marine and Petroleum Geology.* **27** (8), 1765-1774 (2010).
8. Doornhof, D., Kristiansen, T.G., Nagel, N.B., Pattillo, P.D., Sayers, C. Compaction and subsidence. *Oilfield rev.*, **18** (3), 50-68 (2006).
9. Durham, W.B., Weidner, D.J., Karato, S. New developments in deformation experiments at high pressure. *Rev. Mineral. Geochem.* **51** (1), 22-49 (2002).
10. Fyfe, W.S. The evolution of the Earth's crust: modern plate tectonics to ancient hot spot tectonics? *Chemical Geology.* **23**(1-4), 89-114 (1978).
11. Gerward, L., Mo S., Topso, H. Particle size and strain broadening in energy-dispersive -ray powder patters. *J. Appl. Phys.* **47** (3), 822-825 (1976).
12. Heap, M.J., Farquharson, J.I., Baud, P., Lavallée, Y., Reuschlé, T. Fracture and compaction of andesite in a volcanic edifice. *Bulletin of volcanology.* **77** (6), 55 (2015).
13. Lavina, B., Dera, P., Downs, R.T. Modern X-ray diffraction methods in mineralogy and geosci. *Reviews in Mineralogy and Geochemistry.* **78** (1), 1-31 (2014).
14. Leinenweber, K.D. *et al.* Cell assemblies for reproducible multi-anvil experiments (the COMPRES assemblies). *American Mineralogist.* **97**(2-3), 353-368 (2012).
15. Li, L., Weidner, D.J., Raterron, P., Chen, J., Vaughan, M.T. Stress measurements of deforming olivine at high pressure. *Phys. of the Earth and Planetary Interiors.* **143**, 357-367 (2004).
16. Li, L., Weidner, D.J., Chen, J., Vaughan, M.T., Davis, M., Durham, W.B. X-ray strain analysis at high pressure: Effect of plastic deformation in MgO. *J. App. Phys.* **95** (12), 8357-8365 (2004).
17. Minkoff, S.E., Stone C.M., Bryant S., Peszynska, M., Wheeler, M.F. Coupled fluid flow and geomechanical deformation modeling. *J. Petroleum Sci. and Engineering.* **38** (1), 37-56 (2003).
18. Miyagi, L. *et al.* Deformation and texture development in CalrO 3 post-perovskite phase up to 6 GPa and 1300 K. *Earth and Planetary Sc. Letters.* **268** (3), 515-525 (2008).
19. Morton, R.A., Bernier, J.C., Barras J.A. Evidence of regional subsidence and associated interior wetland loss induced by hydrocarbon production, Gulf Coast region, USA. *Environmental Geology.* **50** (2), 261 (2006).
20. Nagel, N.B. Compaction and subsidence issues within the petroleum industry: From Wilmington to Ekofisk and beyond. *Phys. And Chem. of the Earth, Part A: Solid Earth and Geodesy.* **26** (1-2), 3-14 (2001).
21. Nichols, G. Sedimentology and Stratigraphy. *John Wiley & Sons.* (2009).
22. Nicolas, A., Fortin, J., Regnet, J.B., Dimanov, A., Guéguen, Y., Brittle and semi-brittle behaviours of a carbonate rock: influence of water and temperature. *Geophysical Journal International.* **206** (1), 438-456 (2016).
23. Nishiyama, N., Wang, Y., Sanehira, T., Irifune, T., Rivers, M.L. Development of the multi-anvil assembly 6-6 for DIA and DDIA type high-pressure apparatuses. *High Pressure Research.* **28** (3), 307-314 (2008).
24. Nur, A., Walder, J. Time-dependent hydraulics of the Earth's crust. *The role of fluids in crustal processes.* 113-127 (1990).
25. Paterson, M.S. Rock deformation experimentation. The brittle-ductile transition in rocks. The Heard Volume. *The American Geophysical Union, Geophys. Monograph.* **56**, 187-194 (1990).
26. Peng, S.D. Stresses within elastic circular cylinders loaded uniaxially and triaxially. *Int. J. Rock Mech. Min. Sci. Geomech. Abst.* **78** (1), 399-432 (1971).
27. Raterron, P., Merkel, S., Holyoke III, C.W., Axial temperature and gradient and stress measurements in the deformation D-DIA cell using alumina pistons. *Rev. of Sci. Instr.* **84** (4), 043906 (2013).
28. Raghavan, R., Chin, L.Y. Productivity changes in reservoirs with stress-dependent permeability. In SPE Annual Technical Conference and Exhibition. *Soc. of Petroleum Engineers.* (2002).

29. Reynolds, C.A., Menke, H., Andrew, M., Blunt, M.J., Samuel, K. Dynamic fluid connectivity during steady-state multiphase flow in a sandstone. *Proceedings of National Academy of Sci.* **114** (31), 8187-8192 (2017).

30. Scholle, P. A. A color illustrated guide to constituents, textures, cements, and porosities of sandstones and associated rocks. *AAPG Memoir.* No 552.5 SCH (1979).

31. Scholle, P.A., Ulmer-Scholle, D.S. A Color Guide to the Petrography of Carbonate Rocks: Grains, Textures, Porosity, Diagenesis. *AAPG Memoir.* **77** (2003).

32. Scholz, C.H. Experimental study of the fracturing process in brittle rock. *J. Geophys. Res.* **73** (4), 1447-1454 (1968).

33. Schutjens, P.M.T.M. *et al.* Compaction-induced porosity/permeability reduction in sandstone reservoirs: Data and model for elasticity-dominated deformation. *SPE Reservoir Evaluation & Engineering.* **7** (3), 202-216 (2004).

34. Simmons, G., and Wang, H. Single Crystal Elastic Constants and Calculated Aggregate Properties. *MIT Press.* Cambridge, MA, 135-160 (1971).

35. Singh, A.K., Balasingh, C., Mao, H.K., Hemley, R.J., Shu, J. Analysis of lattice strains measured under nonhydrostatic pressure. *J. Applied physics.* **83** (12), 7567-7575 (1998).

36. Terzaghi, K.V. Die berechnung der durchlassigkeitsziffer des tones aus dem verlauf der hydrodynamischen spanningsercheinungen. *Sitzungsberichte der Akademie der Wissenschften in Wein. Mathematisch-Naturwissenschaftliche Klasse. Abteilung IIa.* **132**, 125-138 (1923).

37. Wang, Y., Durham, W.B., Getting, I.C., Weidner, D.J. The deformation D-DIA: a new apparatus for high temperature triaxial deformation to pressures up to 15 GPa. *Rev. Sci. Instrum.* **74** (6), 3002-3011 (2003).

38. Wang, Y., Hilairet, N., Dera, P. Recent advances in high pressure and temperature rheological studies. *J. Earth Sci.* **21** (5), 495-516 (2010).

39. Weidner, D.J. *et al.* Characterisation of Stress, Pressure, and Temperature in SAM85, a DIA Type High Pressure Apparatus. *Geophys. Monogr. Ser. AGU.* Washington, D.C., 13-17 (1992).

40. Weidner, D.J., Wang, Y., Vaughan, M.T. Strength of diamond. *Sci.* **266** (5184), 419-422 (1994).

41. Weidner, D.J. Rheological studies at high pressure. *Rev. in Mineralogy and Geochemistry.* **37** (1), 493-524 (1998).

42. Weidner, D.J., Wang, Y., Chen, G., Vaughan, M.T. Rheology measurements at high pressure and temperature. *Properties of Earth and Planetary Materials at High Pressure and Temperature. AGU.* Washington, D.C., 473-482 (1998).

43. Weidner, D.J., Vaughan, M.T., Wang, L., Long, H., Li, L., Dixon, N.A., Durham, W.B. Precise stress measurements with white synchrotron x rays. *Rev. of Sci. Instrum.* **81** (1), 013903 (2010).

44. Weidner, D.J., Li, L., Whitaker, M., Triplett, R. Ultrasonic Acoustic Velocities During Partial Melting of a Mantle Peridotite KLB-1. *J. Geophys. Res: Solid Earth.* (2018).

45. Whitaker, M.L., Baldwin, K.J., Huebsch, W.R. DIASCoPE: Directly integrated acoustic system combined with pressure experiments-A new method for fast acoustic velocity measurements at high pressure. *Rev. Sci. Instrum.* **88** (3), 034901 (2017).